Integrating Discrete Force Cells into Multi-modal Artificial Skin

Philipp Mittendorfer and Gordon Cheng
Institute for Cognitive Systems,Technische Universität München, Germany
Email: see http://www.ics.ei.tum.de

***Abstract*—In this paper, we present a new version of our multi-modal artificial skin, building from hexagonal shaped, intelligent unit cells. Our focus lies on the design of a discrete normal force sensor cell and its integration next to existing sensors for pre-contact, vibration/motion and temperature. The new force cell is cheap and easy to manufacture, scalable in size and force range, and addresses common drawbacks like hysteresis, noise, robustness and bandwidth. We locally sample and pre-process signals at 2.5 kHz and transfer filtered data at 250 Hz, enabling signal to noise ratios above 50 dB. Our rigid unit cells are encapsulated into 3D printed elastomer molds – we now mix hard and soft materials in the epidermal skin layer, in order to support enhanced force sensing. We provide detailed experimental characterization of the new force sensing modality on a custom dynamic test bench.**

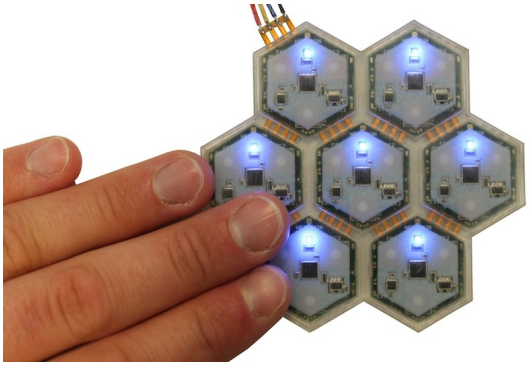

Fig. 1. Skin patch made from 7 hexagonal unit cells with a total of 21 force, 7 acceleration, 14 temperature and 7 proximity/ambient light sensors.

I. INTRODUCTION

A. Motivation

Every interaction of an embodied agent, with itself or the environment, is grounded on its surface. Sensitive skin provides a rich and direct feedback on these interactions, making it a key technology for future robots. Multi-modal awareness of distributed contacts will give robots, commonly only relying on vision and joint force/torque sensors, additional information – e.g. when handling large unknown objects. In order to complete these complex tasks in real-time, sensors must provide reliable and distinct signals, with no or little need for complex signal conditioning stages. Having a closer look at human skin one recognizes that force sensing can be realized with discrete sensor cells. The deformation of the cell is driven by the mechanical behavior of the surrounding skin, accommodating the spatial distance of the discrete sensors and focusing the excitation on the sensitive elements [1]. Discrete sensors are especially useful, when multiple sensor modalities have to share a common space [2]. Analyzing the state of the art, little efforts have gone into the development of a cheap, scalable and robust miniature force sensor that could be easily manufactured and integrated into the automated production process of our multi-modal unit cells. In this paper we describe the design and integration of such a force sensing element.

B. Related Works

The idea of sensitive skin has seen multiple realizations over the past decades [3]. Most physical principles have been exploited to convert excitations, mainly normal forces, into measurable signals. These range from resistive [4] and piezoelectric principles [5], to optical [6] and capacitive effects [7]. The driving touch screen market, and the low power consumption, make capacitive touch sensing technologies most promising. For a force sensitive skin not only the electronic sensing principle, but even more the design of the mechanical conversion mechanism plays a key role. Different materials, like urethane foam [8] or silicone [6], and micro-structures like domes [9] or cantilevers[10], have been utilized to convert forces into measurable displacement. Equally important is the systematic approach [3], dealing with issues like wiring effort, failure tolerance, signal integrity and transferability between robots. Some of these issues have been addressed by our multi-modal skin cell [11].

C. Our Approach

Our new discrete force cell measures the deformation of a circular cavity, etched into a thin copper beryllium (CuBe2) plate, by means of capacitance. These caps can be placed on any quasi-plane, quasi-rigid piece of a substrate material, e.g. a flex-rigid or rigid PCB. In comparison to common, rubber based sensors, this mechanism has significantly better characteristics, due to the behavior of the metal spring (see section III-B). Our force sensor cell is not as complicated and expensive to manufacture, or fragile to use, as state-of-the-art MEMS sensors. On excessive loads, the cell settles into a well defined overload protection state. We also invented a self-adjusting design, in order to minimize the production and thus behavioral differences between a multitude of sensor cells. Substrate and cap can thus be joined in a common, but imprecise, pick&place and reflow soldering process. Our design can be easily scaled to support different sizes and/or force ranges. Here, we combined three sensor cells on our redesigned multi-modal hexagonal unit cell. In order to support force sensing, we enhanced the elastomer cover on top of every unit cell with a harder micro-structure. This

structure distributes forces acting on the surface, focuses the excitation on the three discrete force sensor cells and serves as a protection layer for the embedded electronics.

II. SYSTEM DESCRIPTION

In this section, we first introduce the design of our multi-modal intelligent unit cell. We then continue with a description of the new force sensor cell and its subsystems.

A. Unit Cell

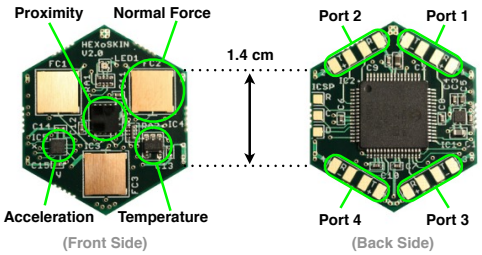

Fig. 2. Multi-modal, intelligent HEX-o-SKIN unit cell. Front side with 4 sensor modalities. Back side with micro controller and 4 power/data ports.

What we refer to as HEX-o-SKIN unit cell is a hexagonal shaped, rigid, printed circuit board (PCB) with 4 sensor modalities on the front side, a local controller and four combined data/power ports on the back side (see Fig. 2). An artificial skin is built by placing these unit cells next to each other into a 3D printed elastomer, connecting the neighboring ports with flexible PCBs [11]. In comparison to the previous version, we exchanged the local controller, updated all existing sensors, redesigned the elastomer molds and added a new sensor modality - force. The new unit provides enhanced local preprocessing features, e.g. tap/impact detection, which are incorporated as flags into the data packets.

B. Discrete Force Sensor

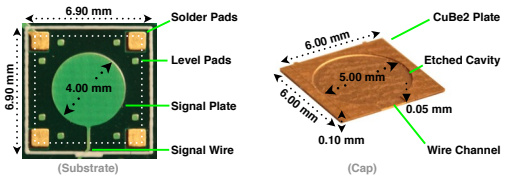

Fig. 3. Substrate and cap design of the new force sensor cell. Placing the cap on the substrate builds a circular cavity which deforms on normal force.

1) **Parts:** The new discrete force sensor cell consists of two main components (see Fig. 3): 1) a conductive, thin and deformable cap with a micro-structured cavity; 2) a plane and rigid substrate with a conductive plate. The cap is made from a (t_{plate} = 100μm) thick CW101C-R1060 copper beryllium (CuBe2) sheet in a fast and cheap lithographic etching process. CuBe2 has excellent spring properties, high corrosion resistance, low creep and good conductivity. It is commonly used for spring contacts or high precision instruments. CuBe2 can be joined with common copper pads on a PCB in a standard soft solder process. We are able to utilize an initially hardened alloy which does not change characteristics during the solder process, due to the low stress put on the material during the etching process. With HEX-o-SKIN, the substrate consists of an ordinary (t_{subs} = 0.85mm) thick FR4 PCB which, compared to the cap, is quasi-plane and -rigid. The actual capacitive sensor element builds from two conductive plates - a circular pad on the PCB and the overlaying part of the metal cap (see Fig. 4).

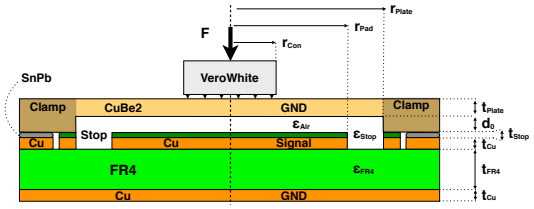

Fig. 4. Axial cut through a simplified, rotatory symmetric force cell model.

2) **Assembly:** Our goal was to integrate the new force cell into the automated fabrication process of the unit cells - utilizing pick&place machines and a reflow soldering process. Therefore, we invented[1] a special design, so the cap self-aligns, relative to the substrate, during the soldering step. This is important as the mechanical pick&place joining process is much less accurate than the chemical/lithographic manufacturing processes for the substrate and the cap. The self-alignment is based on capillary effects, acting in between the cap and the solder pads through the liquid solder. This serves to reduce two sources of uncertainty: 1) to align the cavity and the wire channel horizontally above the signal plate and the signal wire; 2) to minimize the vertical offset of the capacitor plate. For the second purpose, we added extra level pads to minimize lifting effects by the liquid solder (see Fig. 3). In comparison to the uncovered solder pads, the signal plate and the level pads are covered with a common, thin solder resistive layer ($t_{stop} \approx 30\mu m$) on top of the copper. This thin isolation layer is important to prevent short circuits with the capacitive sensor. Otherwise both conductors would directly touch each other in case of a high load condition. The thickness of the solder resistive layer ideally also defines the thickness of the solder joints in between the CuBe2 cap and the solder pads. Here, we control the volume of solder with the solder mask.

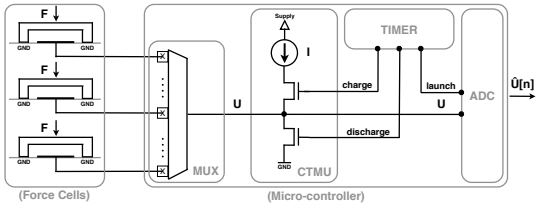

Fig. 5. Conversion electronics used with the PIC24F: Analog multiplexer, charge time measurement unit, timer and analog digital converter.

[1]Patent pending.

3) **Electronics:** In order to reduce components, we make use of the charge time measurement unit (CTMU), a capacitive touch sensing module, built into the PIC24F. The CTMU provides a programmable and switchable constant current source, directly linked to the timer and the analog to digital converter (ADC) (see Fig. 5). The CTMU allows to generate a constant current I, the timer to accurately gate the charge time T and the ADC to measure the final voltage value U. The CTMU can me multiplexed to any of the 16 available analog inputs and measure the capacitance of an attached capacitor. Given that the capacitor has been discharged before, the total capacitance can be directly calculated as:

$$C_{total} = \frac{Q}{U} = \frac{I \cdot T}{U} \tag{1}$$

We use the maximum current $I_{max} = 55\mu A$, allowing the highest update rates and giving resistive parasitic effects least time to interfere. The maximum voltage $U_{max} = 3.0V$ is limited by the supply voltage and the ADC range. The maximum voltage is measured in case of an unloaded sensor cell. Once the capacitor plates are forced together, the capacitance increases. Keeping the charge Q constant, the voltage U decreases. A range optimization algorithm could thus maximize the charging time in the unloaded case - generating custom values T_{cus} for each force cell. Here, we utilize a heuristic default time $T_{def} = 2.5\mu s$, for both charging and discharging times, so we can easily compare raw signals from different cells. The initial capacitance of the force sensor and all parasitic capacitors, like from the pin or ADC, thus sum up to an initial value of $C_{init} = 46pF$. With a sample rate of 200 kHz at 12 bit resolution, one analog to digital conversion approximately takes $T_{ADC} \approx 5\mu s$. A complete force measurement approximately takes $T_{force} \approx T_{ADC} + 2 \cdot T_{def} \approx 10\mu s$. A unit cell could such sample all three force cells with an update rate of $f_{max} = 33kHz$. We currently use a sample rate of $f_{samp} = 2.5kHz$, filter and decimate to the lower transmission rate $f_{tran} = 250Hz$. The digital filter in combination with the oversampling rate serves two purposes: I) as a low-pass filter to obey Nyquist sampling theorem; II) to filter uncorrelated noise and increases the signal to noise ratio. For us, filtering in the digital domain is more effective. We save analog components, reduce costs and parasitic effects, can re-program the filter and achieve steeper filter curves. Filtering in control systems is generally avoided due to the inherent phase shifts. Utilizing unfiltered data, unwanted aliasing and spikes could occur. In consequence, we decided to utilize a non-linear median filter on the last $N = 10$ samples. Median filters do not degrade edges, but efficiently reduce outliers. In our case with $N = 10$ and a following decimation by the same factor, the worst case phase shift for a step response is half of the update rate $\frac{1}{2f_{tran}} = 2ms$. Computation wise, the median calculation[2] takes $T_{med} = 65\mu s$ for all three cells on the PIC24F. Since sampling is handled by a timer triggered, non-interrupt routine, small amounts of sample rate jitter occur. A reasonable amount of sample rate jitter is an effective measure against harmonic noise (refer to [12]) and such desirable.

[2]kth_smallest(array[],10,5) by N. Wirth, implemented by N. Devillard

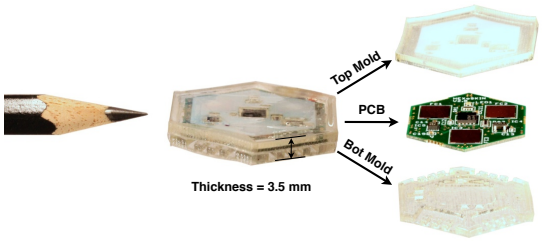

Fig. 6. Parts of the unit cell - Top mold, electronics and bottom mold

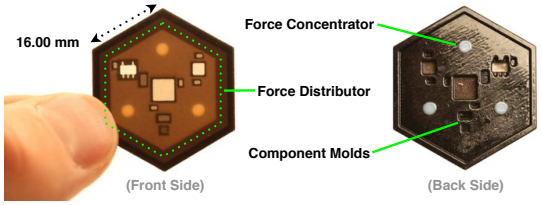

Fig. 7. Micro-structured top cover made of soft TangoPlusBlack and hard TangoGrey material, for enhanced visibility compared to transparent version.

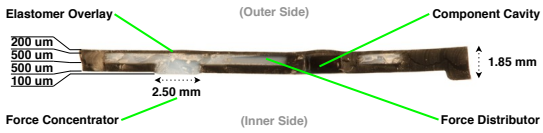

Fig. 8. Vertical cut through the top cover at the center of a force concentrator pillar, showing the micro structure of the composite material.

4) **Composite Skin:** *Composite skin* is the material encapsulating the unit cells (see Fig. 6). The material splits into a top and a bottom mold, with a negative imprint of the unit shape and its components. The bottom mold encapsulates the infrastructure electronics and homogenizes loads acting between the unit cell and the support plane. The top mold encapsulates 4 types of sensor modalities, of which all have to be taken into account during the design. The infrared proximity sensor requires optical transmission of infrared light and limited reflection on the skin layer itself. The temperature sensor needs good thermal coupling to the surface and no excessive overlay of thermally insulating material. The vibration sensor requires surface ripples and stickiness to detect slippage and roughness. Discrete force cells require sufficient distribution of forces among and concentration on cells. We print our molds with an Objet Polyjet prototyping machine, which allows us to make custom artificial skin patches in a very short time and with high accuracy (28 μm resolution). The top layer consists of two different materials, a soft TangoPlus Black/Transparent (TPT) rubber like and a hard Vero White/Grey (VW) ABS plastic like material (see Fig. 8). A hard VW layer of $t_{dist} = 500\mu m$ thickness, $t_{over} = 200\mu m$ below the TPT epidermal skin surface, acts

as a collector of distributed pressure. The accumulated force is then concentrated by three pillars on the three available force sensors per unit cell. The pillars extend through the TPT and about t_{tpe} = 100μm on top of the flat inner surface. All other sensor modalities have cutouts in the VW material that are filled with TPT to provide coupling to the skin but less influence with the force cells. The measures given in Fig. 7 are dictated by the size of the off-the-shelf components and the minimal safe structure size (200μm) with the 3D printer.

III. EXPERIMENTS

In this section, we first describe the test stand. We then provide in detail characterization of our force cell on it.

A. Test Stand

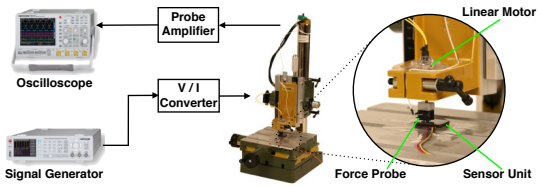

Fig. 9. Custom test stand for dynamic evaluation of artificial skin

Core of our test stand is a VM2836-180 linear voice coil motor (VCM), converting current to force. A LMD18245 current driver converts arbitrary voltage signals from a signal generator, to a regulated current through the VCM. Our test stand currently generates forces between $0.12 - 3.12N$, constrained by the mass of the tip of $12g$ and the VCM maximum current. We directly measure applied forces with a FSG-15N1A sensor at the end of the linear pusher and also utilize its flat, 5 mm diameter tip to press on the skin. The test stand can be extended with a TECB-1 peltier module, to generate higher or lower temperatures.

B. Unit Cell Characteristics

We will now discuss different sets of test data:

1) **Repetitive Signals:** Fig. 10 shows the response towards a burst of sinusoidal or rectangular force pattern, directly applied on cell 3. Quiescent offsets in between the three force cells on the same unit are due to unavoidable differences in the production process, differences in signal wire length and stray capacitance. Permanent offsets can be easily compensated in an automated calibration step. Cross coupling effects could not be discriminated from the noise floor. In order to evaluate the sensor hysteresis, we plotted an overlay of the falling and rising flanks (see Fig. 11). No significant hysteresis could be discriminated.

2) **Step Response:** Fig. 12 shows the response towards a rising and falling step with an amplitude of 3 N directly on cell 3. From this data we calculated mean values μ and standard deviations σ. In case of the excited cell we picked the indicated stable regions with a window length of N_{win} = 300 samples. For cell 1 and 2 we took all (N_{all} = 3995) samples into consideration. We then performed

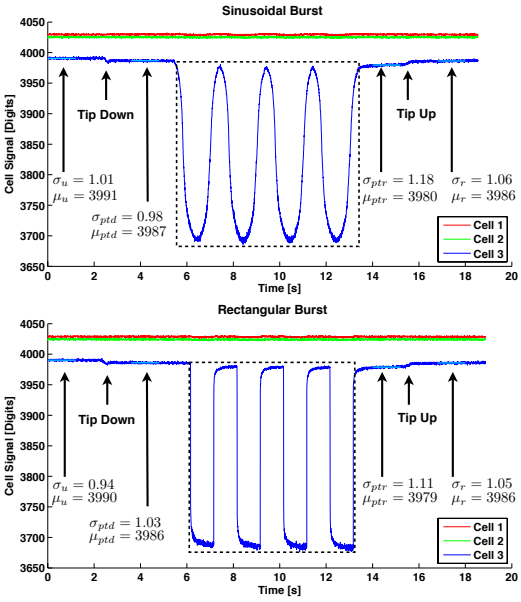

Fig. 10. Response of the unit cell on a burst of 4 sinusoidal or rectangular waves with a force of 0-3.12 N and a 2s period. Arrows are indicating the placement and removal of the force test stand tip with a weight of 12 gram.

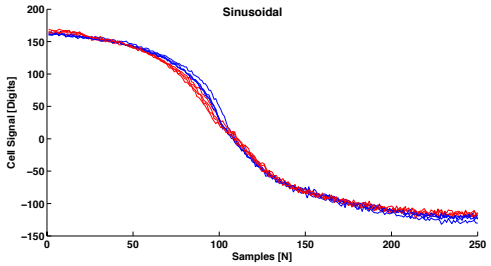

Fig. 11. Overlay plot of the sinusoidal signal flanks in Fig. 10

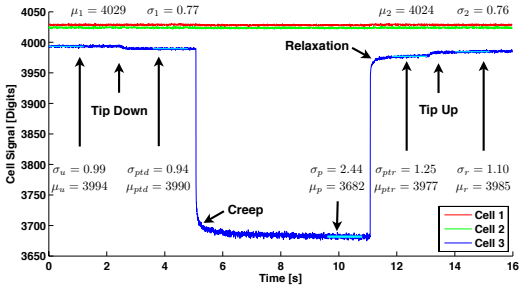

Fig. 12. Response of the unit cell on a single pulse with a force of 0-3 N and a 6s period. Arrows are indicating the placement and removal of the force test stand tip with a weight of 12 gram and regions of special interest.

a Fourier analysis and plotted histograms for all mean free noise signals. Besides gaussian white noise, there was no indication of spectral noise - especially regarding harmonics of the system clock or 50 Hz power net. We then calculated the system span δ, comparing the mean values in the unloaded μ_u and maximally loaded (test stand limit) μ_p state:

$$\delta = |\mu_u - \mu_p| \approx 312 \quad (2)$$

The signal to noise ratio (SNR) can be calculated [12] as:

$$\text{SNR} = \frac{\delta}{\sigma_u} \approx 315 \quad \text{or} \quad \text{SNR}_{db} \approx 20log(\frac{\delta}{\sigma_u}) \approx 49.97dB \quad (3)$$

Conservatively comparing the result to the dynamic range (random signal) or signal to noise ratio (sinusoidal signal) of an analog to digital converter, the resolution would be 8 bit. There is no detectable overshoot or ringing following the step. The sensor signal reaches 70% of the full step span δ within 1 sample period of $T_{s,70} = 4ms$, 90% after $T_{s,90} = 8ms$ and 95% after $T_{s,95} = 36ms$. The fast settling time is due to the specific design of the force cell and the local median filter. A certain amount of creep and relaxation is inherently incorporated by the mixed composite skin, acting as a viscoelastic material. The difference in between σ_u and σ_p can be explained by the vibrations originating from the voice coil motor (audible regulation noise). The difference in between σ_u and σ_r is due to the slight long term relaxation of the difference in between μ_u and μ_r. Top and bottom molds have not yet been glued together, which leads to increased relaxation effects when no load is applied.

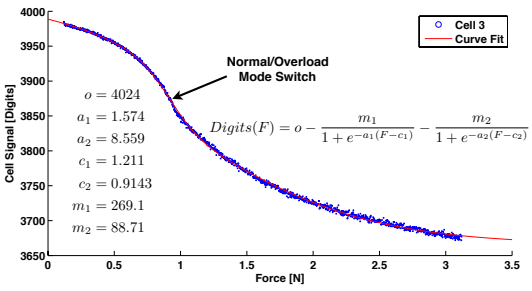

Fig. 13. Curve fitting function and parameters to automatically generate a lookup table for the Force/Digits conversion.

3) **Curve Fitting:** Fig. 13 shows a functional regression model to compute the non-linear mapping in between readings of a force cell and the originating force. A superposition of two sigmoid functions perfectly fits our cell, as their properties (real, differentiable, bounded, ...) match its behavior. Due to the two-split behavior (normal/overload), two sigmoid functions are necessary. Given this differentiable function, it is also possible to express the nonlinear sensitivity $S(F) = \frac{dDigits(F)}{dF}$, which reaches its absolute maximum of $-290\frac{Digits}{N}$ at $F_{sw} = 0.92N$. At this force the cell switches in between normal and overload mode.

4) **Chirp:** Fig. 14 shows the response towards a linear, sinusoidal chirp in between 1 and 250 Hz with a force of 0.12 to 3.12 N directly on cell 3. The visible decay in amplitude is a superposition of the mechanical characteristics of the skin and the non-linear median filter. One has to keep in mind that median filters truncate sinusoidal waveforms dependent on their frequency, whereas they have less distortion effects on steps. It is also visible that the sensor almost reaches full scale values for all frequencies, but does not return to quiescent state for higher frequencies. This shows that

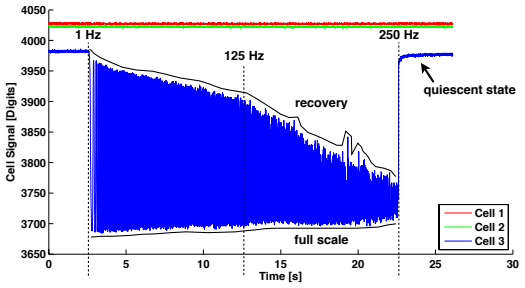

Fig. 14. Response of the force cell 3 on a linear sinusoidal chirp from 1 Hz to 250 Hz, with a force of 0.12-3.12 N and a period of 20s.

the recovery time of the given system, including the mass of the force test stand tip, or any other object applying varying forces, is higher than the reaction time. The system such settles close to full scale deflection, instead of mean or quiescent state. Such a behavior is advantageous for an artificial skin as it detects applied peak forces that can cause harm to objects under manipulation or the robot itself (please see III-B7). Outliers in the data are due to imperfections of the test stand, e.g. the excitation of harmonics in the voice coil motor linear mechanics (especially the guidance slider).

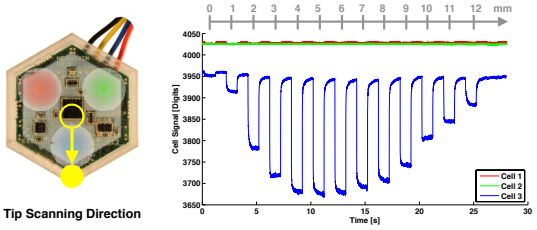

Fig. 15. Receptive fields and response of force cell 3 towards a rectangular excitation, with a force between 0.12-3.12 N and a period of 2s, while shifting the excitation along the indicated direction during low force phases.

5) **Receptive Field:** Fig. 15 shows the measured receptive field of a force cell 3. The receptive field was sampled, scanning with the tip of the force test stand along the indicated line over the surface of the unit cell. We applied a rectangular excitation of 0.12-3.12 N and shifted the position of the tip by one millimeter during each low force phase, making it slightly asymmetric. Ideally the receptive fields of the three cells would overlap such that no insensitive areas remain and every stimulus is sufficiently received by at least one receptor cell. Comparing the expansion of the receptive fields (see Fig. 15 red/green/blue circles), of approximately 12mm, with the size of the unit cell in Fig. 2, it is clear that there are still insensitive areas with the current design and object size (test stand tip). This puts a certain limit to the size and/or curvature radius of objects that can be detected. The final goal of completely overlapping receptive fields could be reached by increasing the thickness of the skin, stiffening the force distributor or by a denser set of smaller sensor cells.

6) **Thermal Variation:** Fig. 16 shows the deviation in response to the same force stimulus at different temperatures.

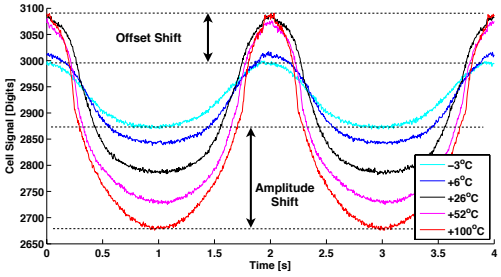

Fig. 16. Response of force cell 3 towards a sinusoidal excitation, with a force between 0.12-3.12 N and a period of 2s, at different temperatures.

In order to avoid bounding constraints, we reduced the charge time to $T_{red} = 1.875\mu s$. Thermal energy was sinked and sourced on the back side of the skin and measured with the LM71 sensor in the upper layer. Such a setup produces temperature gradients, which is much more realistic than a homogeneous distribution. Condensation at low temperatures was prevented with a thin foil on top of the unit cell. The plot contains all possible effects, from the electronics, over thermal stress in the cap and PCB material, to the changing behavior of the composite skin. Significant offsets only occur with low temperatures, which can be explained with the change of elastomer stiffness at low temperatures. Its damping effect can then no longer be neglected and relaxation offsets occur. The amplitude shift can be approximated (0.98 r-square goodness) with a linear model of $-1.9\frac{Digits}{^\circ C}$ gain. One explanation is the thermal increase of capacitive area, explaining lower ADC readings with higher temperatures.

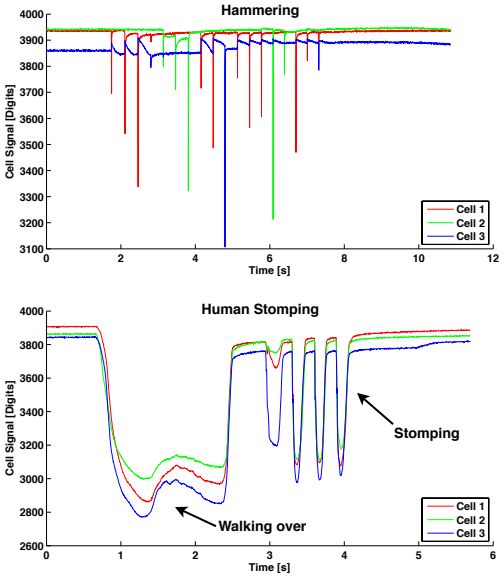

Fig. 17. Unit cell under excessive loads (80 kg human walking over and stomping on unit) and impacts (hammering unit at different locations).

7) **Robustness:** Fig. 17 shows the reaction of a unit cell towards excessive loads and impacts generated by a human walking over, stomping or hammering on a unit cell lying on the floor [3]. Due to the high stress, the composite skin shows slightly more, but reversible relaxation effects. Permanent offsets were not experienced. Deviations in the quiescent state between Fig. 17 and e.g. Fig. 10 are due to the utilization of a different unit cell. The increased system span $\delta \approx 1000$ also indicates the existence of a third, ultrahigh overload mode, with a completely collapsed force cell.

IV. CONCLUSION

In this paper, we introduced a cheap, scalable, discrete force cell and means to easily integrate it, along with other (discrete) sensor modalities, into a multi-modal artificial skin. An in depth analysis with a dynamic force test stand was presented. In comparison to the referenced state of the art, our sensor has a low hysteresis, can endure high overloads without damage, has a high and programmable bandwidth (≥ 250Hz) and high signal to noise ratio (≥ 50dB). We demonstrated the design of an artificial skin, optimized towards multiple coexisting (discrete) sensor modalities - independent of size and utilized technology.

Acknowledgment

This work was supported (in part) by the DFG cluster of excellence 'Cognition for Technical systems - CoTeSys'.

REFERENCES

[1] T. Maeno, K. Kobayashi, and N. Yamazaki, "Relationship between the structure of human finger tissue and the location of tactile receptors," *JSMA International Journal*, vol. 64, no. 628, pp. 4798–4805, 1998.

[2] P. Mittendorfer and G. Cheng, "Uniform cellular design of artificial robotic skin," *7th German Conference on Robotics*, pp. 145–149, May 2012.

[3] R. S. Dahiya, G. Metta, M. Valle, and G. Sandini, "Tactile sensing-from humans to humanoids," *IEEE Transactions on Robotics*, vol. 26, pp. 1–20, February 2010.

[4] H. Alirezaei, A. Nagakubo, and Y. Kuniyoshi, "A tactile distribution sensor which enables stable measurement under high and dynamic stretch," *IEEE Symposium on 3D User Interfaces*, pp. 87–93, March 2009.

[5] D. Göger, N. Gorges, and H. Wörn, "Tactile sensing for an anthropomorphic robotic hand - hardware and signal processing," *IEEE International Conference on Robotics and Automation*, pp. 895 – 901, 2009.

[6] A. Persichetti, F. Vecchi, N. Vitiello, T. Lenzi, and M. C. Carrozza, "Skilsens: conformant and robust sensing skin," *Workshop on Tactile Sensing in Humanoids - Tactile Sensors and Beyond, Humanoids*, 2009.

[7] G. Cannata, M. Maggiali, G. Metta, and G. Sandini, "An embedded artificial skin for humanoid robots," *Proceedings of IEEE International Conference on Multisensor Fusion and Integration for Intelligent Systems*, pp. 434–438, August 2008.

[8] Y. Ohmura, Y. Kuniyoshi, and A. Nagakubo, "Conformable and scalable tactile sensor skin for curved surfaces," *International Conference on Robotics and Automation*, pp. 1348–1353, 2006.

[9] W.-Y. Tseng, J. S. Fisher, K. Rinaldi, and A. P. Lee, "A slow-adapting microfluidic based tactile sensor," *IEEE 21st International Conference on Micro Electro Mechanical Systems*, pp. 912 – 915, January 2008.

[10] C. M. Oddo, L. Beccai, M. Felder, F. Giovacchini, and M. C. Carrozza, "Artificial roughness encoding with a bio-inspired mems-based tactile sensor array," *Sensors*, pp. 3161–3183, 2009.

[11] P. Mittendorfer and G. Cheng, "Humanoid multi-modal tactile sensing modules," *IEEE Transactions on Robotics*, vol. 27, no. 3, pp. 401–410, June 2011.

[12] B. Davison, "Techniques for robust touch sensing design," AN1334 Microchip Technology Inc., 2010.

[3] Please also refer to our video submission.